Experimental studies of α-AlD_3 and α′-AlD_3 *versus* first-principles modelling of the alane isomorphs†

Sabrina Sartori,*[a] Susanne M. Opalka,[b] Ole Martin Løvvik,[ac] Matylda N. Guzik,[a] Xia Tang[b] and Bjørn C. Hauback[a]

Received 6th December 2007, Accepted 25th February 2008
First published as an Advance Article on the web 5th March 2008
DOI: 10.1039/b718896j

The thermal phase behaviour of cryomilled α′-AlD_3 and α-AlD_3 was investigated by *in situ* synchrotron powder X-ray diffraction (SR-PXD), differential scanning calorimetry and first principles atomic modelling. *In situ* measurements showed that α′-AlD_3 decomposes directly into Al and D_2 at around 80 °C during heating at 1 °C min^{-1}. At higher temperatures the transformation of α′-AlD_3 to α-AlD_3 was observed by DSC measurements at 5 °C min^{-1}, and tentatively by *in situ* SR-PXD at 1 °C min^{-1}. Atomic modelling was carried out to investigate possible structural relationships and transformation pathways between the α- and α′-phase. Group–subgroup relation analyses and direct method lattice dynamics were used to rule out a possible displacive transformation pathway between the α′- and α-phases. The likelihood of a reconstructive transformation was demonstrated by partial transformation of an interface between α′ and α domains during elevated temperature molecular dynamics. Such an α′- to α-phase transformation may be possible when kinetic barriers can be overcome at elevated temperatures or during long time periods. These insights are also relevant to the transformation mechanisms of the β-AlD_3 and γ-AlD_3 isomorphs to the α-phase.

1. Introduction

The search for solid state hydrogen storage materials is one of the key technological challenges in the transition towards the implementation of a hydrogen economy.[1–3] Aluminium hydride (AlH_3, alane) contains 10.1 wt% of hydrogen and a theoretical H density of 148 g L^{-1}. This significant H capacity offers promise for hydrogen storage applications. AlH_3 has been found to adopt at least six different crystal structures (α, α′, β, γ, δ and ε) depending on the synthesis route.[4] The structure of α-AlH_3 has been known for some time.[5] Recently the accurate structures of α′, β and γ modifications have been determined by powder neutron diffraction.[6–8] Numerous investigations have been conducted on the thermodynamic and decomposition behaviour of the α, β and γ alane phases.[4,9–20] The recent investigations[12–20] have been motivated by the goal to establish fundamental understanding of AlH_3 reaction mechanisms to set the stage for improving its H storage on-board reversibility and/or off-board regeneration. α-AlH_3 is the most stable modification with a dehydrogenation enthalpy, determined by calorimetry, to be 5.7–7.6 kJ mol^{-1} H_2.[9,10,14,15] It has been reported that the α form of AlH_3 releases hydrogen at temperatures above 60 °C,[4,11,13] whereas γ-AlH_3 slowly releases hydrogen during storage at the room temperature.[4] The release of hydrogen from the β and the γ phases proceeds first *via* formation of α-AlH_3 followed by its decomposition.[16] However, the direct decomposition of the γ-phase to Al has also been observed.[16,20]

α-AlH_3 is metastable at room temperature.[12] Al and H_2 are the thermodynamic products of the decomposition and the reaction is not reversible at moderate conditions.[12] A re-hydrogenation pressure of more than 100 kbar at room temperature[21,22] suggests to develop an off-board regeneration of hydrogen in AlH_3.

AlH_3 has typically been synthesized from $LiAlH_4$ and $AlCl_3$ in diethyl ether. By adding $LiAlH_4$ or $LiBH_4$, the ether is removed and AlH_3 crystallizes usually in the α, β or γ structure depending on the conditions.[4] Nonsolvated α′-AlD_3 was obtained by ethereal solutions of AlH_3 containing excess of $LiAlH_4$, when heated under pressure at 70–80 °C.[4] The nonsolvated α′-phase did not appear to convert to α-AlH_3 but was much less thermally stable than the α form.[4]

A much simpler method to synthesize the α and α′-modifications by advanced ball milling at liquid nitrogen temperature (cryomilling) has been recently reported by Brinks *et al.*[6,23] In this case, $LiAlD_4$ and $AlCl_3$ were cryomilled in a 3 : 1 ratio and a mixture of about 2/3 α- and 1/3 α′-AlD_3 was obtained together with LiCl.

Recently α′-AlH_3 was predicted to be more stable than α-AlH_3.[24] These findings inspired the current study to evaluate the relative stability and structural relationships between the α′- and α-phases. Thereafter, *in situ* experimental structural and calorimetric studies were carried out to elucidate α′-AlD_3 and α-AlD_3 decomposition behaviour. First-principles minimizations to the ground state, lattice dynamics and molecular dynamic predictions were made in parallel to simulate their physical properties and to probe possible decomposition mechanisms. The experimental and theoretical results were

[a]*Department of Physics, Institute for Energy Technology, P.O. Box 40, NO-2027 Kjeller, Norway. E-mail: sabrinas@ife.no; Fax: +4763810920; Tel: +4763806388*
[b]*United Technologies Research Center, 411 Silver Lane, East Hartford, CT, 06108, USA*
[c]*Department of Physics, University of Oslo, P.O. Box 1048, Blindern, NO-0316, Oslo, Norway*
† This paper is part of a *Journal of Materials Chemistry* theme issue on hydrogen storage and generation. Guest editor: John Irvine.

used to interpret the greater stability of the α-AlD_3 phase and the concurrent behaviour of these phases during decomposition relative to that observed for the β-AlD_3 and γ-AlD_3 phases.

2. Experimental

$LiAlD_4$ (Sigma-Aldrich, >95% chemical purity, >98% isotope purity) and $AlCl_3$ (Merck, 98% purity) were cryomilled in a 3 : 1 ratio. Samples were handled under Ar atmosphere in a glove box and sealed in milling vials to prevent reactions with moisture and oxygen. A Spex 6750 freezer mill with a piston of 32 g was used for cryomilling 1 g of sample at 77 K. For each sample the total milling time was 60 min.

In situ synchrotron powder X-ray diffraction (SR-PXD) measurements were performed at the Swiss–Norwegian beam line (station BM01A) at the European Synchrotron Radiation Facility (ESRF) in Grenoble, France. A small amount of powder was kept in a 0.5 mm boron-silica glass capillary, sealed with graphite and kept under dynamic vacuum. The sample was heated with a hot air blower from room temperature to 180 °C with a constant heating rate of 1 °C min^{-1}. Temperature calibration was performed by measuring a sample of pure Ag.

The SR-PXD patterns (exposure time of 20 s) were collected using an image plate detector (MAR345) and then integrated by the Fit2D program.[25] The wavelength, $\lambda = 0.8082$ Å, and the sample to detector distance, $d = 200$ mm, giving a 2θ range of 1–40° for the one-dimensional diffraction patterns, were calibrated from an individual run with LaB_6.

For selected patterns, Rietveld refinements were performed with the Fullprof software.[26] The peak shapes were described by the pseudo-Voigt function and the background was defined manually for all refined patterns. A sequential mode of refinements was performed for the first 44 patterns.

All crystal structural models used during refinements are listed in Table 1. For all present phases the scale factor, profile, unit cell and atomic displacement parameters were refined. Deuterium coordinates were not refined.

Thermal analyses of the cryomilled AlD_3 were conducted on a TA Instruments 2920 differential scanning calorimeter (DSC). The sample was transferred and hermetically sealed in an Al pan in a glove box with a N_2 gas train. The heat flow of a ~5 mg sample was measured at a heating rate of 5 °C min^{-1} from 25 to 400 °C in a N_2 atmosphere.

Table 1 Refined unit cell parameters for α′-AlD_3, α-AlD_3, LiCl and Al at room temperature are shown. Standard deviations are given in parentheses. Refined atomic coordinates for deuterium are from ref. 6

Atom	*x*	*y*	*z*
α′-AlD_3: space group *Cmcm*, $a = 6.484(4)$ Å, $b = 11.112(3)$ Å, $c = 6.572(1)$ Å.			
Al1	0	0.5	0
Al2	0.25	0.25	0
D1	0	0.197(2)	0.451(4)
D2	0.312(2)	0.1000(14)	0.047(3)
D3	0	0. 465(3)	0.25
D4	0.298(4)	0.277(2)	0.25
α-AlD_3: space group $R\bar{3}c$, $a = 4.4411(6)$ Å, $c = 11.807(3)$ Å.			
Al	0	0	0
D	0.6277(5)	0	0.25
LiCl: space group $Fm\bar{3}m$, $a = 5.1447(4)$ Å.			
Li	0	0	0
Cl	0.5	0.5	0.5
Al: space group $Fm\bar{3}m$, $a = 4.0498(2)$ Å.			
Al	0	0	0

First-principles atomic modelling calculations were carried out on a plane-wave, periodic basis using the density functional theory (DFT) code, Vienna *Ab-initio* Simulation Package (VASP)[27,28] and the regular projector augmented wave potentials[29] with the generalized gradient approximation exchange-correlation functional of Perdew and Wang 91.[30] Accurate precision calculations were made with a plane-wave cutoff of 780 eV, Monkhorst–Pack *k*-point meshes with 0.3 $Å^{-1}$ or finer spacing, and Methfessel–Paxton smearing with an energy broadening of 0.2 eV, with a final energy extrapolation to zero smearing. Minimizations to the ground state were made on candidate bulk and slab structures with an electronic convergence criterion of 1×10^{-6} eV and an atomic force convergence criterion of 0.005 eV $Å^{-1}$.

Direct method lattice dynamic (DMLD) calculations with the harmonic approximation were performed by means of the Phonon program,[31] as implemented in the MedeA simulation interface[32] with displacements of symmetry unique atoms by ±0.002 Å imposing a 0.1 strength of condition factor for translational invariance. Quasi-harmonic volume temperature dependence determinations were not made because they would not have had a significant impact on reducing thermodynamic error. In addition, it has been reported in ref. 24 that lattice dynamics with different size displacements did not produce evidence of anharmonic effects for AlH_3. The integrated predicted phonon density of states were analyzed with statistical mechanical functions to determine the vibrational contributions as a function of temperature. Thermodynamic predictions were derived from the ground state and vibrational contributions using the procedure detailed in ref. 33. Following established methodology,[34] the Commonsubs and Tranpath programs of the Bilbao crystallographic server[35] were used to identify candidate group–subgroup relations and transformation pathways, respectively. VASP quantum-mechanical molecular dynamics 127 and 700 K thermalizations with a micro-canonical ensemble were used to investigate proposed surface decomposition mechanisms and interfacial first-order transformation mechanisms for durations up to 1300 femtoseconds.

3. Results and discussion

3.1 Experimental α′-AlD_3 decomposition analyses

Analyses were made of the cryomilled AlD_3 structural and thermal behavior during heating to gain insight into the relationship between the α′-AlD_3 phase and the other known AlD_3 phases. The two-dimensional *in situ* SR-PXD measurements in Fig. 1 showed that both α′- and α-AlD_3 phases decomposed during heating while the amount of Al increased.

Fig. 2 shows selected Rietveld plots of the sample at intermediate temperatures during heating from room temperature to 180 °C at a heating rate of 1 °C min^{-1}. Quantitative phase analysis on the sample at room temperature indicated the presence of five phases: α′-AlD_3, α-AlD_3 (relative ratio $\alpha'/\alpha = 0.67$), LiCl and traces of β-AlH_3 and metallic Al. Due to its negligible amount, the β-phase was not considered in the Rietveld

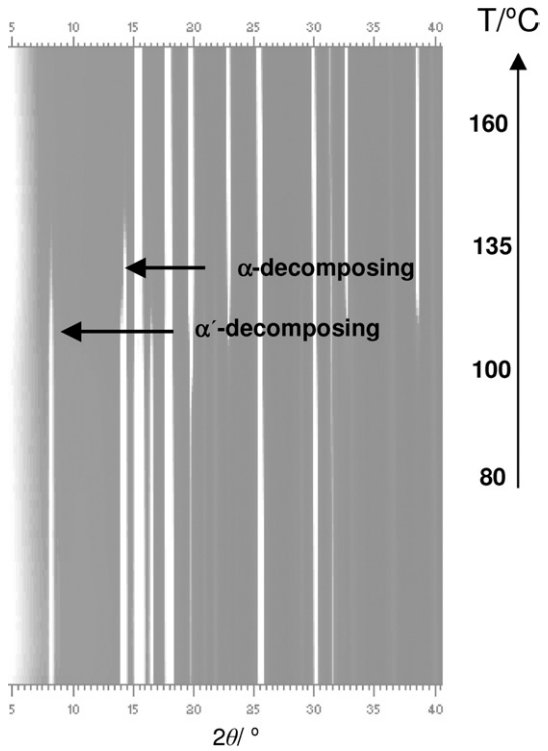

Fig. 1 Two-dimensional *in situ* SR-PXD data during heating showing the decomposition of the alane phases.

refinement and thus is not shown in the calculated patterns. The relative amounts of α′-, α-AlD_3 and Al analyzed from the SR-PXD patterns in the temperature range from 60 to 180 °C are shown in Fig. 3. Below 95 °C, α′-AlD_3 is transformed directly to Al and D_2. At higher temperatures α′-AlD_3 is completely decomposed and only traces of α-AlD_3 can be detected at 165 °C. The expanded inset in Fig. 3 shows that α′-AlD_3 starts to slightly decompose at about 80–85 °C (Fig. 3). In this temperature region no increase in the intensity for the α-phase and a slight increase of the Al intensity is observed. This suggests a direct decomposition of α′-AlD_3 into Al at these temperatures, according to:

$$\alpha'\text{-}AlD_3 \xrightarrow{80\ ^\circ C} Al + 3/2D_2 \qquad (R1)$$

The decomposition of α-AlD_3 starts at 95–100 °C and can be observed up to 160 °C (Fig. 3). DSC, thermal desorption spectroscopy (TDS) and SR-PXD investigations have shown, in previous publications, decomposition temperatures for the α-phase between 130 and 170 °C.[15–17,20] The increased brittleness of the material during the cryomilling could lead to reduced particle sizes which can affect the decomposition temperature for the α-phase obtained in the present work.

The cryomilled α′-AlD_3 thermal behaviour differs from the decomposition reported for the β- and γ-AlD_3 isomorphs. The β-AlD_3 obtained by wet chemistry transforms into the α-phase before decomposing to Al following the reaction pathway:[16,20]

$$\beta\text{-}AlD_3 \xrightarrow{80\ ^\circ C} \alpha\text{-}AlD_3 \xrightarrow{130\ ^\circ C} Al + 3/2D_2 \qquad (R2)$$

However, the behaviour described by R1 can be compared to the direct decomposition of γ-AlD_3 (also obtained by wet

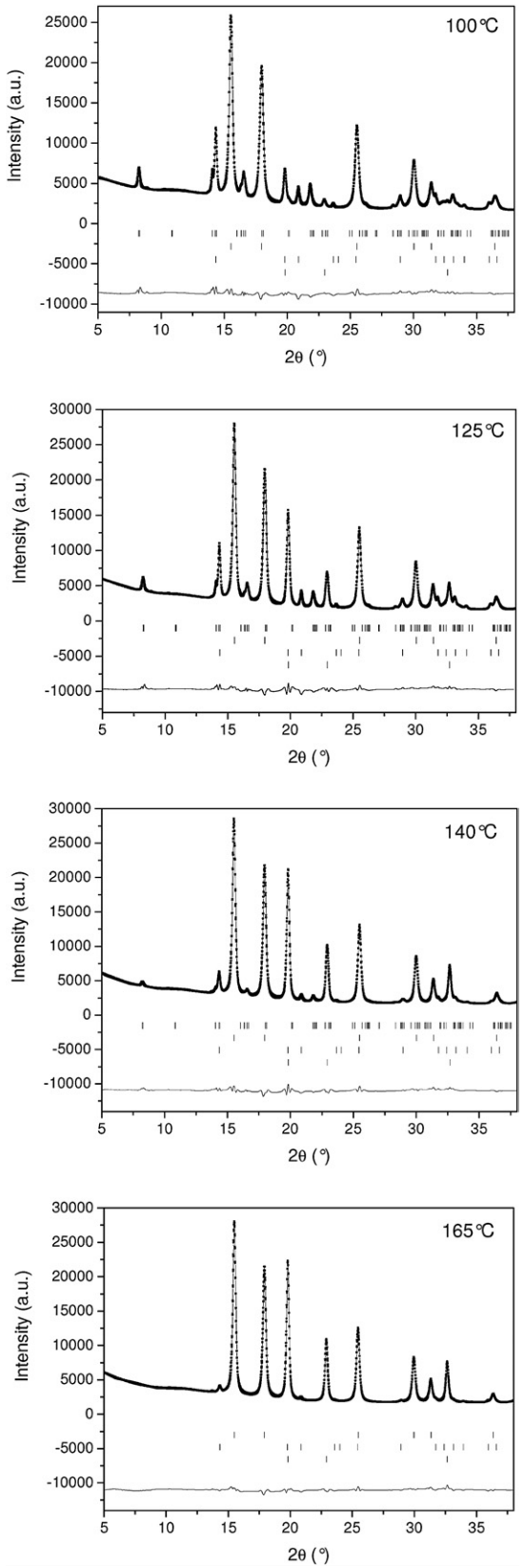

Fig. 2 *In situ* SR-PXD patterns from Rietveld refinement at selected temperatures during thermal decomposition of the sample showing observed (points), calculated (upper line) and difference (bottom line) plots. The positions of the Bragg peaks are shown as ticks (from top to bottom: α′-AlD_3, LiCl, α-AlD_3, Al). At 165 °C the phases are LiCl, α-AlD_3, and Al.

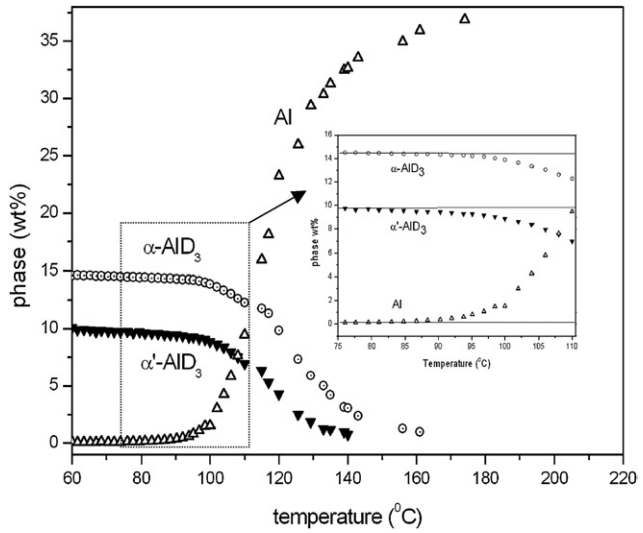

Fig. 3 Phase fractions from the Rietveld refinements of the *in situ* SR-PXD patterns of the sample during the thermal decomposition.

chemistry) to aluminium at 110 °C (R4) that can be observed together with a phase transformation to the α polymorph followed by its decomposition, according to the following equations:[15–18,20]

$$\gamma\text{-AlD}_3 \xrightarrow{90\ ^\circ C} \alpha\text{-AlD}_3 \xrightarrow{130\ ^\circ C} \text{Al} + 3/2\text{D}_2 \qquad \text{(R3)}$$

$$\gamma\text{-AlD}_3 \xrightarrow{110\ ^\circ C} \text{Al} + 3/2\text{D}_2 \qquad \text{(R4)}$$

Differential thermal analyses conducted on the cryomilled AlD_3 at a 5 °C min^{-1} heating rate revealed similar phase behaviour to that already determined for the β- and γ-AlD_3 isomorphs.[15,17] An exothermic reaction that onset at ~70 °C and peaked at 132 °C (Fig. 4) is attributed to the transformation of α′-AlD_3 to the α-AlD_3 phase. The integrated exothermic peak corresponds to a transformation enthalpy, $\Delta H_{transform}$, of 1.6 kJ mol^{-1} AlD_3. This is very close to what has been reported by Graetz and Reilly[15] for β-AlH_3. These results show that α′-AlD_3 can transform to α-AlD_3 under certain temperature and heating rate conditions. Above 140 °C, a decomposition endotherm with a peak at 146 °C and two shoulder peaks was observed. This is similar to the single decomposition endotherm reported

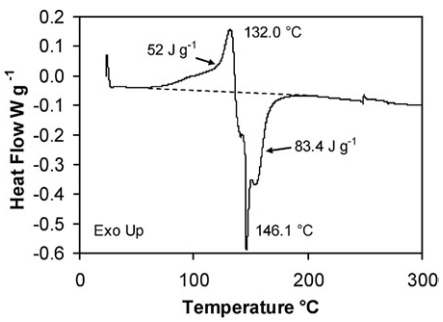

Fig. 4 Differential scanning calorimetry plot for the cryomilled sample in the temperature range of 25–300 °C ramped at a rate of 5 °C min^{-1}.

for α-AlD_3.[15,17] The lower peak decomposition temperature measured (146 °C *versus* 170 °C) is most probably due to the slower heating rate used in the analyses, compared to the 10 °C min^{-1} analyses conducted by Graetz and Reilly,[15] even though some effect of autocatalysis due to the use of an Al crucible can not be excluded.

In situ SR-PXD decomposition studies of α-AlH_3 obtained by wet chemistry has been reported.[20] In this case a significant anisotropic volume expansion of α-AlH_3 during heating was observed with the main expansion proceeding along the *a* unit cell axis and thus elongations of the bridging bonds Al–H–Al aligned along [1$\bar{1}$1/2].

The evolution of the unit cell parameters for the α′- and α-phases as a function of temperature are shown in Fig. 5 and 6, respectively. Both phases display an anisotropic expansion of the unit cell over the whole temperature range, with almost unchanged *a*-axis for α′-AlD_3 and *c*-axis for α-AlD_3. The *b*- and *c*-axes for α′-AlD_3 expand almost linearly with the temperature, although *c* shows three regions: linear expansion from the room temperature to about 100 °C; almost constant up to 120 °C; and linear expansion in the range 120–140 °C.

For α-AlD_3 the changes in unit cell axes are in agreement with *in situ* SR-PXD decomposition studies of samples synthesized by wet chemistry methods.[16,20] The beginning of the region where values of the *c*-axis of the α′-phase remain constant coincides with the temperature range where the α-phase starts to decompose.

3.2 Theoretical investigations

3.2.1 Alane phase thermodynamic predictions. Fig. 7 shows the first coordination spheres of the AlH_6 octahedra as well as the unit cells of the four alane phases studied theoretically: the orthorhombic α′-AlH_3, the trigonal α-AlH_3, the cubic β-AlH_3, and the orthorhombic γ-AlH_3, respectively.[6–8] The isomorphic structures, shown in Fig. 7, all contain 3 center Al–H–Al mixed covalent–ionic bonds, which are intermediate in character between metal hydrides and complex hydrides. The isomorphs differ from one another by the tilting of the octahedra, which are noted in Table 2 using the Woodward notation,[36] and the interconnectivity between neighbouring octahedra in the first coordination sphere. The vertice-sharing interconnections in the first coordination sphere are: zero in the α-AlH_3 phase, 4 out of 6 in the α′-AlH_3 phase, and all 6 in the β-AlH_3 phase.[6,7] In the γ-AlH_3 phase, 4 out of 8 octahedra in the first coordination sphere share edges.[8] The α′-phase can hence be regarded as an intermediate between the α- and β-phases. Also, the densities of the structures are different. While α-AlH_3 has the smallest volumes of all the alane isomorphs, with a volume per AlH_3 unit of 33.5 $Å^3$ and a density of 1.487 g cm^{-3}, α′-AlH_3 is less dense, with 39.3 $Å^3$ and a density of 1.27 g cm^{-3}, due to hexagonal pores with a diameter of 3.9 Å through the structure. The transformation from β-AlH_3, with 45.6 $Å^3$, density 1.092 g cm^{-3} and connectivity between the octahedra that gives rise to channels of about 3.9 Å diameter, should involve rearrangements of the AlH_6 octahedra for a transformation to the α-AlH_3 together with a compression in the unit cell to eliminate the channels. In addition to corner-sharing octahedral, γ-AlH_3 also has edge-sharing octahedra. For the transition from γ- to

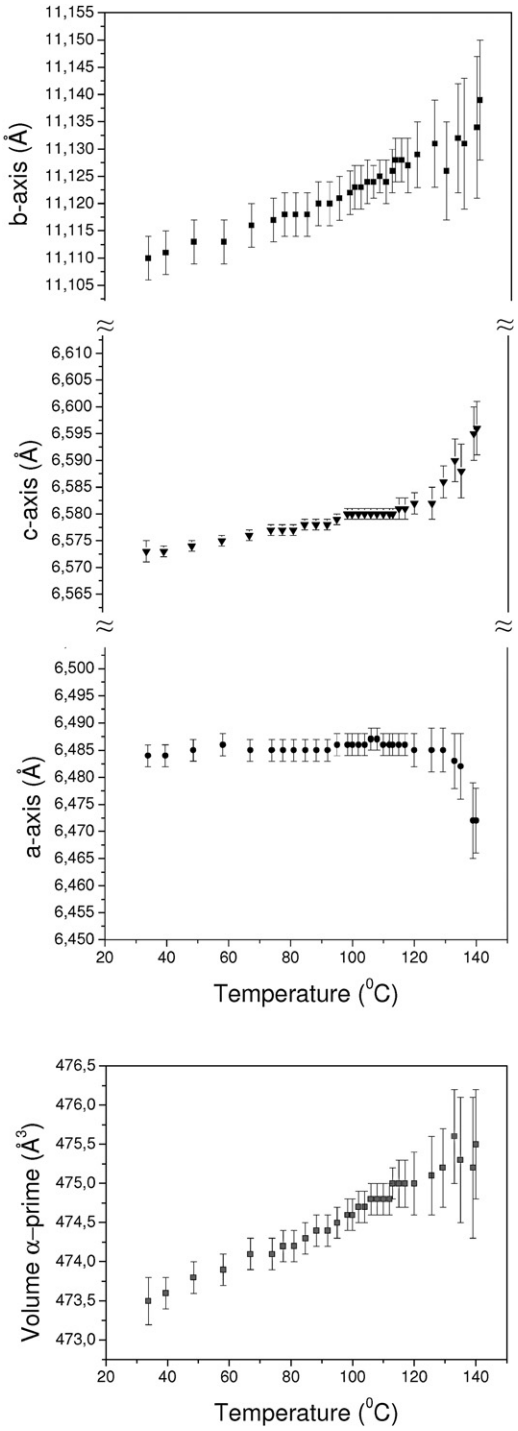

Fig. 5 Changes in dimensions of unit cell and volume *vs.* temperature for the α′-phase calculated from the *in situ* SR-PXD patterns of the sample during the decomposition.

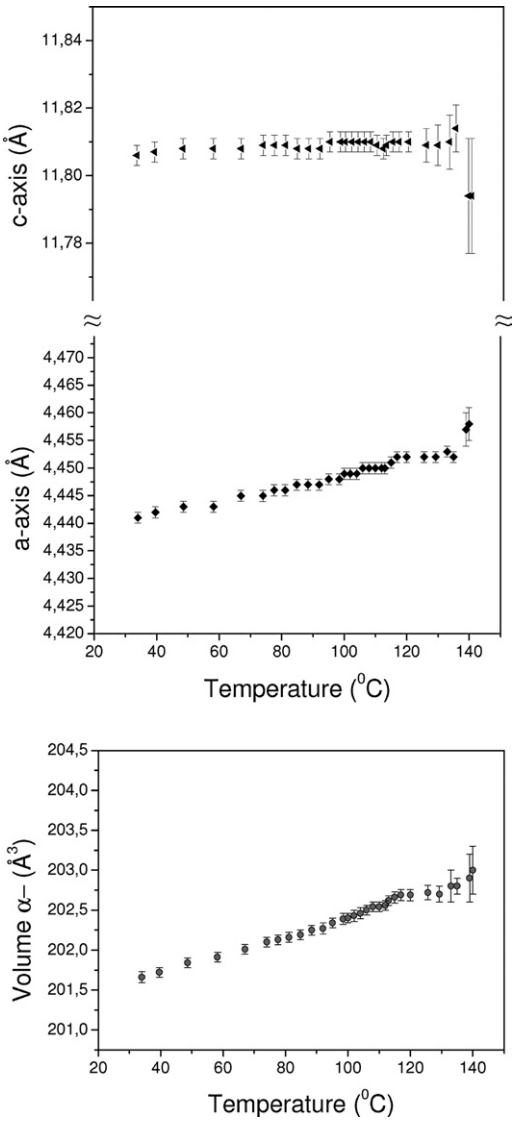

Fig. 6 Changes in dimensions of unit cell and volume *vs.* temperature for the α-phase calculated from the *in situ* SR-PXD patterns of the sample during the decomposition.

α-AlH_3, an analogous shrinkage should happen to the cavities in the *ab*-plane of γ-AlH_3, which is characterized by a volume of 37.8 Å^3 and density of 1.319 g cm^{-3}.[16]

The structurally known α- $R\bar{3}c$, α′- *Cmcm*, β- $Fd\bar{3}m$ and γ- *Pnnm* AlH_3 isomorphs were simulated to enable a baseline comparison with other experimental and theoretical results prior to the investigation of alane transformation mechanisms. The VASP minimized lattice parameters for the 4 AlH_3 isomorphs shown in Fig. 7 are listed in Table 2. They are all within 1.5% of the experimentally refined values.[6–8] The DMLD predicted and measured AlH_3 thermodynamic parameters are given in Table 3. The predicted Gibbs free energy of formation at 298 K of the α-phase agrees well with the theoretical values of 49.8 kJ mol^{-1} and 44.9 kJ mol^{-1}, and the experimental value of 46.5 kJ mol^{-1}.[9,24,37] Even though H–D isotope effects have been identified in previous modeling studies on complex hydrides, this gave relatively small changes in the calculated Gibbs energy for different phases (in the order of a few kJ mol^{-1}; within the typical error bar of such calculations).[38]

The Gibbs predicted values for the different phases do not cross one another with increasing temperature, indicating that first order type latent heats are necessary for transformations between phases. The predicted values for the α′-, β- and γ-AlH_3 phases were corrected with their respective latent heats for transformation to the α phase, measured by DSC in this

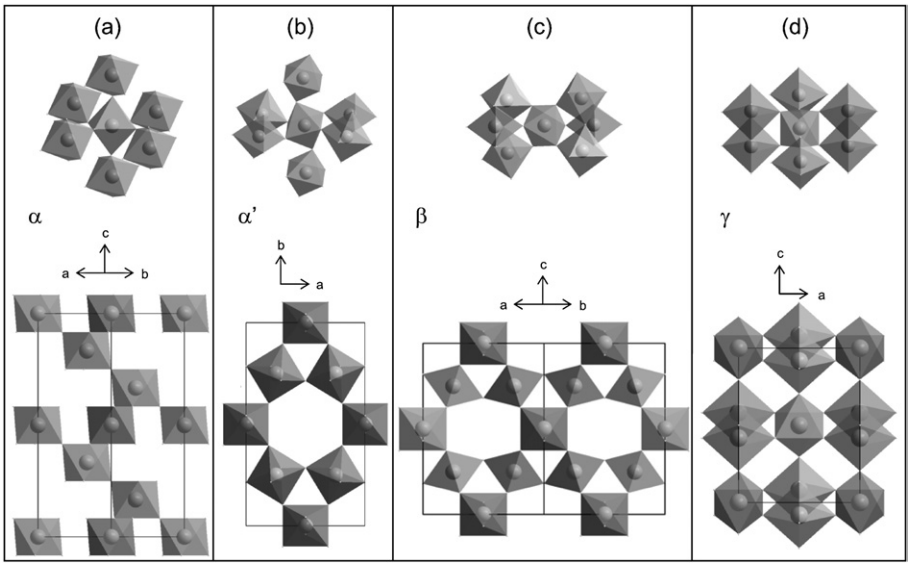

Fig. 7 The first coordination sphere for the octahedral units (upper part) and the unit cell (lower part) of the (a) α-, (b) α′-, (c) β- and (d) γ-phases of AlH_3.

Table 2 Predicted minimized AlH_3 phase unit cell parameters. Also shown are the tilting of octahedra in the Woodward notation and the number of formula units per conventional unit cell Z

	Minimized unit cell parameters								
AlH_3 phase	a	b	c	α/β	γ	Al–H/Å	Vol. per atom/Å^3	Tilt	Z
α $R\bar{3}c$	4.4805	4.4805	11.8137	90.0	120.0	1.7201	8.5579	$a^-a^-a^-$	6
α′ $Cmcm$	6.5266	11.1419	6.6074	90.0	90.0	1.7181	10.0100	$a^0b^+c^-$	12
β $Fd\bar{3}m$	9.0668	9.0668	9.0668	90.0	90.0	1.7215	11.6463	$\sim a^0a^0a^0$	16
γ $Pnnm$	7.4126	5.4401	5.7989	90.0	90.0	1.7183/1.7583	9.7433	$\sim a^0b^-a^0$	6

Table 3 Thermodynamic measurements and predictions [kJ (mol AlH_3)$^{-1}$] for the alane isomorphs

AlH_3 phase	Measured $\Delta H_{transform}$	Measured ΔG_{form} (298 K)	Predicted ΔG_{form} (298 K)
α $R\bar{3}c$	—	48.5[a]	45.9
α′ $Cmcm$	1.6	ND	44.0
β $Fd\bar{3}m$	1.5[a]	50.5[a]	43.7
γ $Pnnm$	2.8[a]	51.4[a]	49.2

[a] Ref. 15.

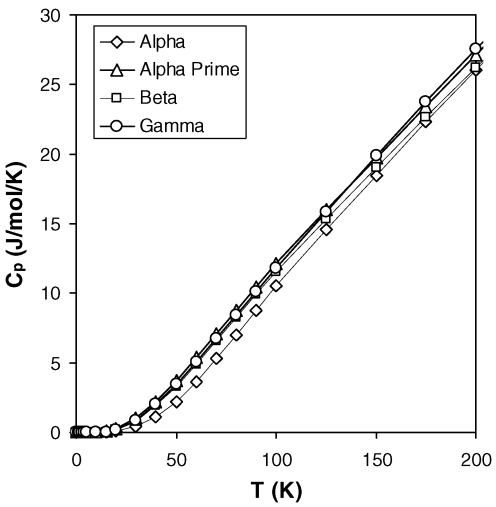

Fig. 8 Predicted finite temperature heat capacity values for AlH_3 isomorphs.

study for the α′-phase and in ref. 15 for the β- and γ-isomorphs. These corrections reduce somewhat the predicted differences in stability of these phases relative to the α-phase, so that at least the γ-phase is predicted to be less stable than the most stable α-phase. The differences in the predicted stability between the phases are very small and indistinguishable considering the typical prediction accuracy of 5–15 kJ mol^{-1} for DFT thermodynamic predictions.[39–42] Since the vibrational properties from DMLD are not dependent on the absolute position of the potential energy surface, the heat capacity values derived from the vibrational properties are highly accurate.[41] Fig. 8 shows the heat capacity values for all four phases are remarkably close. Any predicted differences in stability are primarily due to the DFT ground state determinations. The failure to predict the α-phase as the most stable phase is probably ascribable to the inherent error in DFT due to the exchange-correlation analytic expression. The insignificant differences in predicted stabilities

for all known isomorphs could be used as an explanation for the multiple alane phases often observed simultaneously in experimentally prepared samples.

3.2.2 Alane bulk lattice stability investigations. The predicted lattice dynamics and structural relationships between the different alane phase space groups were evaluated to look for evidence of possible transformation mechanisms. The predicted phonon dispersion plots in Fig. 9 did not show any negative frequencies for the four alane phases minimized to the ground state, in agreement with the predicted phonon densities of states reported for the structural isomorphs related to the α-, α′- and β-phases.[24] Such negative phonon frequencies or soft modes would be indicative of instabilities to displacive transformations and could be used to map out possible displacive transformation pathways.[31,40] However, soft modes involving large, nonlinear displacements can not be described within the limitations of the DMLD harmonic approximation.[43]

The structural relationships between the alane phases were examined with the Bilbao Crystallographic Server Commonsubs and Tranpath programs[7,35] in order to propose possible displacive transformation pathways for the α′-, β- and γ-phases to the experimentally determined most stable α-phase. Here, a displacive transformation may occur directly between two

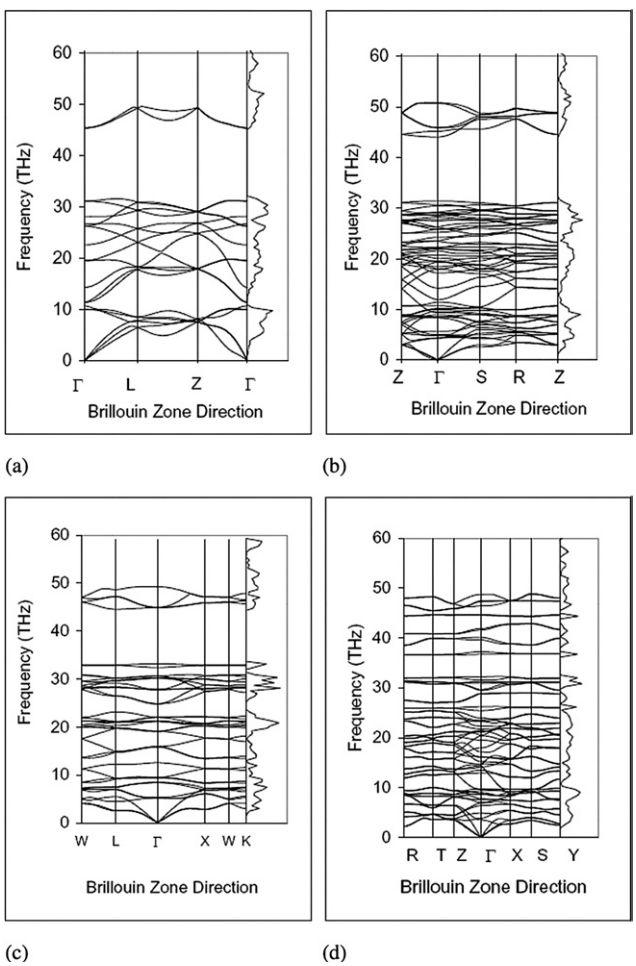

Fig. 9 Phonon dispersion curves for the AlH_3 isomorphs (a) α- $R\bar{3}c$, (b) α′- *Cmcm*, (c) β- $Fd\bar{3}m$ and (d) γ- *Pnnm*.

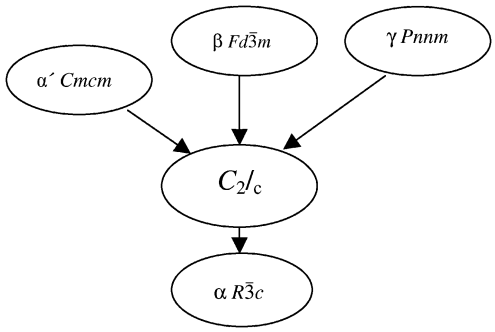

Fig. 10 Schematic for candidate AlH_3 transformation pathway based on maximal group–subgroup relationships.

structures or indirectly by passing through one or more intermediate structurally related symmetries. The latter was found to be the case for the possible transformations under consideration. The highest symmetry common subgroup between the *Cmcm* α′-, $Fd\bar{3}m$ β- or *Pnnm* γ-AlH_3 phases and the $R\bar{3}c$ α-AlH_3 phase was found to be the C_2/c phase. The analyses showed that the C_2/c structure could potentially serve as the single intermediate step for the α′- to α-phase transformation. This relationship is illustrated schematically in Fig. 10. The intermediate C_2/c structure can be derived by imposing a *xx* or *yy* strain on the primitive unit cell of the $R\bar{3}c$ α-phase. The predicted phonon dispersion plot for a minimized C_2/c phase did not exhibit any imaginary frequencies. Further analyses determined that the C_2/c phase could be one of several possible necessary intermediate steps for the more complex β- or γ- to α-phase transformations. The higher connectivity in the first coordination spheres of the β- or γ-phases would require even more complex transformation pathways to the α-phase.

Additional strained structures were minimized from the $R\bar{3}c$ primitive cell for α-AlH_3 and the *Cmcm* α′-phase conventional cell to search for evidence of elastically induced lattice instabilities. Phonon calculations were made on the various strained structures, and the results are summarized in Table 4. It is seen that none of the strained structures exhibit soft modes indicative of displacive instability or transformation.

The likelihood of a displacive transformation from the *Cmcm* α′- to the $R\bar{3}c$ α-phase was of prime interest in this study. The structures for a possible displacive transformation from the *Cmcm* α′-phase through the intermediate C_2/c phase to the $R\bar{3}c$ α-phase are visualized in Fig. 11. Here, the conventional unit cells for the *Cmcm* α′- and the $R\bar{3}c$ α-phases are shown in the upper left and right of Fig. 11, respectively. A 100 × 120 × 100 orthogonal representation of the $R\bar{3}c$ α-phase, as shown in

Table 4 Symmetries obtained by straining the α′- and α-phases in the specified directions

Deformed phases from α′ (*Cmcm*)	Relaxed symmetry	Phonon dispersion
yz strain (C_2/m)	almost *Cmcm*	No soft modes
xz strain (C_2/c)	*Cmcm*	ND
xy strain ($P2_1/m$)	$P2_1/m$	No soft modes
From α ($R\bar{3}c$)		
$xx \cong yy$ strain (C_2/c)	C_2/c	No soft modes

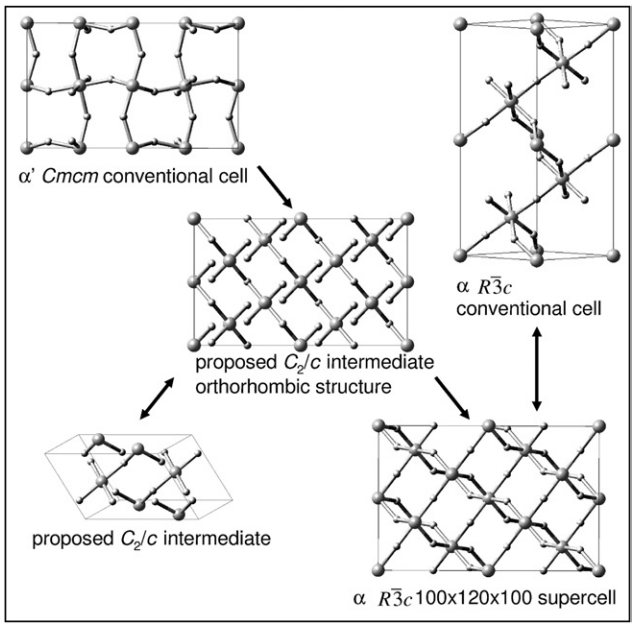

Fig. 11 Structures for candidate α′- to α-AlH_3 displacive transformation pathway.

the lower right of Fig. 11, enables direct comparison of the two phases. The intermediate C_2/c structure from the *xx*- or *yy*-strained $R\bar{3}c$ α-phase primitive cell, as shown in the lower left, can also be visualized by expanding the $R\bar{3}c$ α-phase orthogonal representation (lower right) along the *x* axis to approach the *x* parameter of the *Cmcm* α′-phase conventional cell, as shown in the center.

The Tranpath program was used to search for transformation pathways from the *Cmcm* to the C_2/c structure, and from the C_2/c to the $R\bar{3}c$ structure. However, no pathways were predicted, because the transformations would have required unreasonably large changes in atomic positions that are atypical for displacive transformations. If the structures in Fig. 11 are examined more closely, it is clear why such a displacive transformation is unlikely. In order for the α′- to transform to the α-phase, the AlH_6 octahedra would need to tilt alternately, to shift laterally in varying magnitude, and to break vertex sharing in the first coordination sphere. This would require breaking of bonds and rearrangement of the atoms typical of a reconstructive or diffusional-type transformation. The kinetic barriers to such a transformation may be high relative to decomposition to the elemental phases. This may explain why the α′- to α-phase transformation was observed at intermediate temperatures at the faster DSC heating rate of 5 °C min^{-1}, but only tentatively at the slower SR-PXD heating rate of 1 °C min^{-1}. The exothermic transformation to the α-phase is likely to be kinetically limited at low temperatures and thermodynamically limited (less favourable) at high temperatures. The direct endothermic decomposition to Al and H_2 would become kinetically competitive with increasing temperature and decreasing heating rate. The same rationale could be relevant to phase behaviour of the β- or γ-phases, where their increased interconnectivity may serve to further kinetically impede their transformation to the α-phase.

3.2.3 Alane surface and interfacial stability investigations. Surface slabs of the α- and α′-phases were used to simulate surface stability and decomposition reactions. Two low-index surfaces were chosen for each of the phases, representing the most close-packed surfaces with a minimal number of Al–H bonds broken per surface unit area: the (001) and (1$\bar{1}$0) surfaces of the α-phase, and the (001) and (210) surfaces of the α′-phase. Due to the sixfold coordination of Al, a few possibilities emerge for the number of hydrogen atoms pointing out of the surface N_{Hout} for each of the surfaces. The different options used in this study are shown in Fig. 12, where for instance the possibilities N_{Hout} = 0, 1, 2, and 3 are shown for the α-phase (001) surface. Stoichiometry of the slab was retained by adjusting N_{Hout} of the opposite side of the slab.

The surface energy of each of these surface terminations was calculated using a linear fit to an increasing number of slab layers as the bulk energy, as originally proposed by Boettger.[44] The bottom layer was fixed to the bulk minimized parameters and upper layers were relaxed to represent the solid/air interface. The resulting surface energies are presented in Table 5.

We first note that the lowest surface energies of the α (001) surface are obtained for N_{Hout} = 1 or 2. This means that Al atoms at the surface most probably will not be fully coordinated, and that small particles will not be completely filled with H. We

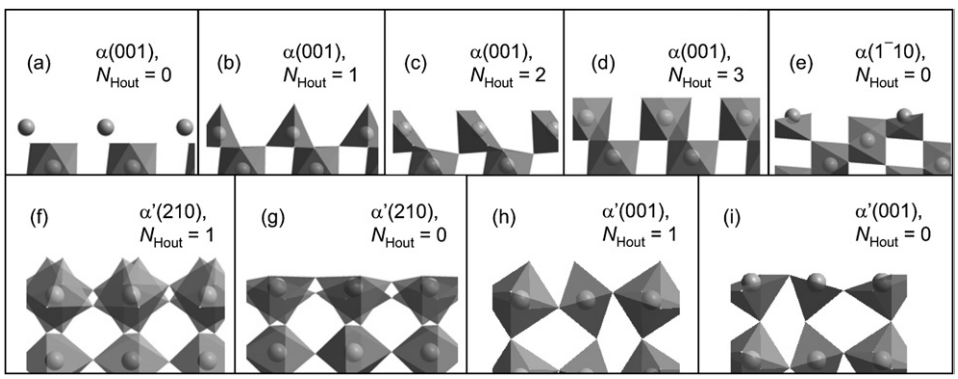

Fig. 12 Side-view of the surfaces investigated by modeling in this study: α (001) with the number of hydrogen atoms pointing out of the surface N_{Hout} = 0 (a), N_{Hout} = 1 (b), N_{Hout} = 2 (c), and N_{Hout} = 3 (d); α (1$\bar{1}$0) with N_{Hout} = 0 (e); α′ (210) with N_{Hout} = 1 (f) and N_{Hout} = 0 (g); α′ (001) with N_{Hout} = 1 (h) and N_{Hout} = 0 (i). The number of layers was six for all the slab models.

Table 5 Surfaces of the α′- and α-phases investigated in this study. N_{Hout} is the number of hydrogen atoms pointing out of the surface, and E_{surf} is the converged surface energy in J m^{-2}. t_{rel} is the elapsed time during the molecular dynamics simulation before the onset of the first H_2 dissociation from the surface. The time step was 1.3 fs

Surface	N_{Hout}	E_{surf}/J m^{-2}	t_{rel}/fs (@400 K)	t_{rel}/fs (@700 K)
α (001)	0	1.65	>700	>700
	1	0.69	>700	>700
	2	0.68	>700	>700
	3	1.53	39	17
α (1$\bar{1}$0)	1	0.70	>700	>700
α′ (001)	0		>700	>700
	1	1.18	104	59
α′ (210)	0		>700	>700
	1	1.58	151	33

shall see this demonstrated later, when turning to molecular dynamics of these surfaces. For the remaining surfaces only the surface energy of terminations with $N_{Hout} = 0$ or 1 are presented. The relaxed surfaces with $N_{Hout} = 0$ or 1 are all quite similar, with one hydrogen atom pointing perpendicularly out of the surface, even if this was not the case in the bulk cut structure.

The surface energies of the two α-phase surfaces are both in the order of 0.7 J m^{-2}, which is remarkably low. This may help to explain the apparent metastability of the α-phase under ambient conditions. Prior reports have attributed the stability of α-AlH_3 under ambient conditions to the passivation of nanocrystallites by adsorbed surface (hydro-)oxide layers,[4,12] but there is no direct experimental evidence supporting this. The α′-phase surfaces we studied are not as stable, with more typical surface energies around 1.3 and 1.6 kJ mol^{-1}. This is consistent with the experimental observation that 30% of the α′-phase decomposes at 40 °C in two weeks,[6] while exhibiting similar thermodynamic stability as the α-phase. The cryomilled sample considered in this paper was stored under argon at room temperature and after 28 weeks the relative ratio α′/α = 0.5 was measured, while the amount of Al increased of almost 30%. These differences could not easily be explained by surface (hydro-)oxide layers, since there is no reason why the α and α′-phases should be affected differently by such layers. We thus believe that the high surface stability of α-AlH_3 is the primary reason for its metastability.

To investigate this further, quantum-mechanical molecular dynamics were made at 127 and 427 °C for all the surfaces mentioned above. The time steps were 1.3 fs, and up to 1000 time steps were performed for each surface. Some of the surfaces released one or more H_2 molecules during this period, and the time before the onset of such release t_{rel} is included in Table 5. We see that the very low surface energies are reflected in an extraordinary stability of the α surfaces. Even at 427 °C no H_2 is released from these surfaces during the entire simulation of at least 700 fs. The lower stability of the α′-phase surfaces was also reflected through the molecular dynamics. Surfaces with $N_{Hout} = 1$ started losing H_2 molecules very rapidly, both at 127 and 427 °C. No further degassing was seen during the remaining simulation. The simulation time was of course much less than the time scales that may be involved in the decomposition of these materials. Also, the decomposition mechanisms at low temperatures may be different from those at higher temperatures. Nevertheless, the loss of H_2 from these surfaces may be seen as the first step of the decomposition of the α′-phase at lower temperature.

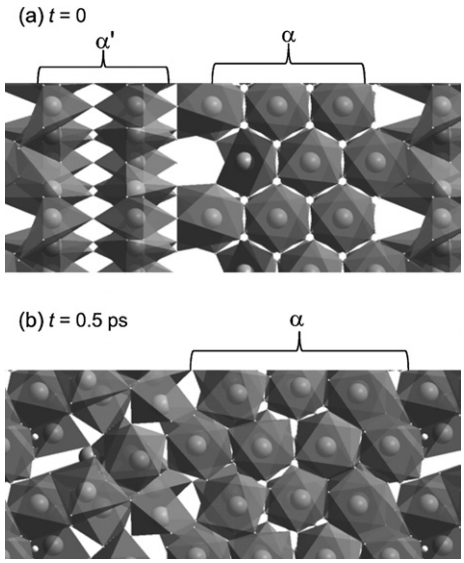

Fig. 13 Model interface between α-AlH_3 (1$\bar{1}$0) and α′-AlH_3 (001) sections. The input model (a) is compared to the model after 500 fs molecular dynamics simulation (b).

The surfaces above are all perfect, and clearly not reflecting the variety of surfaces present in real samples. To mimic more realistic surfaces, molecular dynamics were also made on the α-phase (1$\bar{1}$0) surface after removing various surface groups. The surface was still very stable: removal of 1 H, 2 H or AlH_3 from the surface did not lead to further dehydrogenation or significant reconstruction for up to 800 fs at 127 °C. Removal of Al and H only led to dissociation of H_2 during the simulation.

Finally, molecular dynamics was conducted on a model interface between the α′ and α phase domains to simulate a possible reconstructive transformation mechanism. The input model is shown in Fig. 13a: it consists of an unrelaxed α′-phase (001) surface slab interfaced with an unrelaxed α-phase (1$\bar{1}$0) surface slab. Since the intent was to prompt the α′-phase reconstruction to the α-phase, the interface was constructed by adjusting the cross-sectional (x and y) dimensions of the α′- (001) slab to match those of the α-phase (1$\bar{1}$0) slab. The slabs were joined so that the closest interfacial Al–H bond distances were similar to those within the respective bulk phases. The resulting structure after 500 fs simulation at 127 °C is shown in Fig. 13b. Partial reconstruction took place with the α-phase domain increasing at the expense of the α′-phase. It may be concluded that the transformation between α′- and α-phases may take place at transforming boundaries such as the one studied here, but are likely to be kinetically activated at elevated temperatures.

4. Conclusions

The stability of α-AlD_3 and α′-AlD_3 obtained by cryomilling has been investigated experimentally and interpreted theoretically. *In situ* SR-PXD showed that α′-AlD_3 decomposes directly into Al and D_2 in the temperature range 80–95 °C at a heating rate of 1 °C min^{-1}. At higher temperatures the transformation of

α′-AlD_3 to α-AlD_3 was observed by DSC measurements at 5 °C min^{-1}, and tentatively by *in situ* SR-PXD at 1 °C min^{-1}. Group–subgroup relation analyses and direct method lattice dynamics were used to rule out a possible displacive transformation pathway between the α′- and α-phases. The likelihood of a reconstructive transformation was demonstrated by partial transformation of an interface between α′- and α-domains during elevated temperature molecular dynamics.

A consistent picture from the experimental and modelling efforts is as follows: the kinetically slow transformation between the α′- and α-phases at room temperature could be possible during long term storage. During heating at low temperatures, the α′-phase is directly decomposed into the elements where the kinetic barrier between the α′- and α-phase is too high for the exothermic transformation to take place. The kinetic barriers are overcome at intermediate temperatures, enabling the transformation to the α-phase to precede the decomposition. The transformation is thermodynamically limited at even higher temperatures where the endothermic decomposition increases in kinetic activity. The α-phase exhibits surfaces with very low surface energy and very high stability during molecular dynamics simulations, which alone can explain the metastability of this phase during long term room temperature storage, as well as the relatively higher stability of this phase at higher temperatures compared to the other isomorphs of alane.

Acknowledgements

Financial support from the project StorHy with contract number SES6-CT-2004-502667 under the FP6 Energy Program in the European Commission is acknowledged. The skilful assistance from the project team at the Swiss–Norwegian Beam Line, ESRF, Grenoble, is also gratefully acknowledged. S. M. Opalka and X. Tang acknowledge support by the U.S. Department of Energy Contract DE-FC04-02AL66710. Financial support from the NANOMAT program in the Research Council of Norway (grant no. 158516/S10) and computational resources from the NOTUR project are gratefully acknowledged by O. M. Løvvik. We are grateful for the important discussions and advice from Paul Saxe of Materials Design Inc.

References

1 L. Schlapbach and A. Züttel, *Nature*, 2001, **414**, 353.
2 W. Grochala and P. P. Edwards, *Chem. Rev.*, 2004, **104**, 1283.
3 A. Züttel, *Mater. Today*, 2003, **Sept**, 24.
4 F. M. Brower, N. E. Matzek, P. F. Reigler, H. W. Rinn, C. B. Roberts, D. L. Schmidt, J. A. Snover and K. Terada, *J. Am. Chem. Soc.*, 1976, **98**, 2450.
5 J. W. Turley and H. W. Rinn, *Inorg. Chem.*, 1969, **8**, 18.
6 H. W. Brinks, A. Istad-Lem and B. C. Hauback, *J. Phys. Chem. B*, 2006, **110**(51), 25833.
7 H. W. Brinks, W. Langley, C. M. Jensen, J. Graetz, J. J. Reilly and B. C. Hauback, *J. Alloys Compd.*, 2007, **433**(1–2), 180.
8 H. W. Brinks, C. Brown, C. M. Jensen, J. Graetz, J. J. Reilly and B. C. Hauback, *J. Alloys Compd.*, 2007, **441**(1–2), 364.
9 G. C. Sinke, L. C. Walker, F. L. Oetting and D. R. Stull, *J. Phys. Chem.*, 1967, **47**, 2759.
10 P. Claudy, B. Bonnetot and J. M. Letoffe, *Thermochim. Acta*, 1978, **27**, 205.
11 P. J. Herley and O. Christofferson, *J. Phys. Chem.*, 1981, **85**, 1882.
12 G. Sandrock, J. J. Reilly, J. Graetz, W. M. Zhou, J. Johnson and J. Wegrzyn, *Appl. Phys. A*, 2005, **80**, 687.
13 J. Graetz and J. J. Reilly, *J. Phys. Chem. B*, 2005, **109**, 22181.
14 S. Orimo, Y. Nakamori, T. Kato, C. Brown and C. M. Jensen, *Appl. Phys. A*, 2006, **83**, 5.
15 J. Graetz and J. J. Reilly, *J. Alloys Compd.*, 2006, **424**, 262.
16 H. Grove, M. H. Sørby, H. W. Brinks and B. C. Hauback, *J. Phys. Chem. C*, 2007, **111**, 16693.
17 J. Graetz, J. J. Reilly, J. G. Kulleck and R. C. Bowman, *J. Alloys Compd.*, 2007, **446–447**, 271.
18 S. J. Hwang, Jr., R. C. Bowman, J. Graetz, J. J. Reilly, W. Langley and C. M. Jensen, *J. Alloys Compd.*, 2007, **446–447**, 290.
19 J. Graetz, S. Chaudhuri, Y. Lee, T. Vogt, J. T. Muckerman and J. J. Reilly, *Phys. Rev. B*, 2006, **47**, 214114.
20 J. P. Maehlen, V. A. Yartys, R. V. Denys, M. Fichtner, Ch. Frommen, B. M. Bulychev, P. Pattison, H. Emerich, Y. E. Filinchuk and D. Chernyshov, *J. Alloys Compd.*, 2007, **446–447**, 280.
21 B. Baranovski and M. Tkacz, *Z. Phys. Chem. (N. F.)*, 1983, **135**, 27.
22 S. K. Konovalov and B. M. Bulychev, *Inorg. Chem.*, 1995, **34**, 172.
23 H. W. Brinks and B. C. Hauback, Institute for Energy Technology, *Norwegian patent application*, 2006, No. 062210 and *International patent application*, 2007, No. PCT/NO007/00173.
24 X. Ke, A. Kuwabara and I. Tanaka, *Phys. Rev. B*, 2005, **71**, 184107.
25 A. P. Hammersley, FIT2D V12.077; Internal Report ESRF-97-HA02 T, 1997; Internal Report ESRF-98-HA01 T, 1998.
26 J. Rodriguez-Carvajal, *Fullprof Suite*, LLB Saclay & LCSIM, Renne, France, 2003.
27 G. Kresse and J. Hafner, *Phys. Rev. B*, 1993, **47**, 558.
28 G. Kresse and J. Furthmüller, *J. Comput. Mater. Sci.*, 1996, **6**(1), 15.
29 G. Kresse and D. Joubert, *Phys. Rev. B*, 1999, **59**, 1758.
30 J. P. Perdew, J. A. Chevary, S. H. Vosko, K. A. Jackson, M. R. Pederson, D. J. Singh and C. Fiolhais, *Phys. Rev. B*, 1992, **46**, 6671.
31 K. Parlinski, Z. Q. Li and Y. Kawazoe, *Phys. Rev. Lett.*, 1997, **78**, 4063.
32 K. Parlinski, MedeA-Phonon Version 1.0 using Phonon Software 3.11, © 1998–2006 Materials Design, Inc., Angel Fire, NM.
33 C. Qiu, S. M. Opalka, G. B. Olson and D. L. Anton, *Int. J. Mater. Res.*, 2006, **97**, 845.
34 J. M. Perez-Mato, M. Aroyo, A. García, P. Blaha, K. Schwarz, J. Schweifer and K. Parlinski, *Phys. Rev. B*, 2004, **70**, 214111/1.
35 M. I. Aroyo, A. Kirov, C. Capillas, J. M. Perez-Mato and H. Wondratschek, *Acta Crystallogr., Sect. A*, 2006, **62**, 115.
36 P. M. Woodward, *Acta Crystallogr., Sect. B*, 1997, **53**, 32.
37 C. Wolverton, V. Ozoliņš and M. Asta, *Phys. Rev. B*, 2004, **69**, 144109.
38 T. J. Frankcombe and G. J. Kroes, *Chem. Phys. Lett.*, 2006, **423**, 102.
39 O. M. Løvvik, S. M. Opalka, H. W. Brinks and B. C. Hauback, *Phys. Rev. B*, 2004, **69**, 134117.
40 S. M. Opalka, O. M. Løvvik, H. W. Brinks, P. W. Saxe and B. C. Hauback, *Inorg. Chem.*, 2007, **46**, 1401.
41 C. Qiu, S. M. Opalka, G. B. Olson and D. L. Anton, *Int. J. Mater. Res.*, 2006, **97**, 1484.
42 http://www1.eere.energy.gov/hydrogenandfuelcells/pdfs/storage_theory_session_opalka.pdf.
43 W. Wolf, J. Sticht, A. Mavromaras, B. Leblanc, P. Saxe and E. Wimmer, *Mater. Sci.*, 2005, **23**(2), 365.
44 J. C. Boettger, *Phys. Rev. B*, 1994, **49**, 16798.

